

Transworld Research Network  
37/661 (2), Fort P.O., Trivandrum-695 023, Kerala, India



Recent Advances in Hyperspectral Signal and Image Processing, 2006:  
ISBN: 81-7895-218-1 Editor: Chein-I Chang

---

# Applications of morphological processing to endmember extraction

---

**Antonio J. Plaza**

Computer Science Department, University of Extremadura, Avda. de la Universidad s/n, 10071 Caceres, Spain

## Abstract

*Mathematical morphology is a non-linear technique for spatial image analysis that has found many applications in different areas. This chapter reports on the extension of morphological image processing to hyperspectral imagery. In order to define extended morphological operations, a physically meaningful distance-based vector organization scheme is introduced, and fundamental vector operations are defined by extension. A specific application of extended morphological transformations is explored in this chapter: the*

---

Correspondence/Reprint request: Dr. Antonio J. Plaza, Computer Science Department, University of Extremadura, Avda. de la Universidad s/n, 10071 Caceres, Spain. E-mail: [aplaza@unex.es](mailto:aplaza@unex.es)

*morphological identification of pure spectral constituents (endmembers) for mixed pixel characterization. Multi-channel morphological transformations demonstrate excellent performance when compared to other hyperspectral analysis methodologies in this particular application. A quantitative and comparative performance study in relation to available techniques, using real hyperspectral imagery collected by the 224-channel NASA/Jet Propulsion Laboratory Airborne Visible-Infrared Imaging Spectrometer (AVIRIS), reveals that the complementary utilization of spatial and spectral information by the proposed transformations alleviates the problems related to each of them taken separately. The chapter also develops a parallel implementation that speeds up computational performance.*

## 1. Introduction

Mathematical morphology (MM) is a theory for spatial structure analysis, which began as a geometry-based study of binary porous media in France in the mid-sixties [1]. An overview of the developments of MM at the *Centre de Morphologie Mathématique* from the early days of morphology can be found in [2]. MM started to broaden its audience in 1982 when Jean Serra published the first monograph devoted to MM [3]. It has now evolved into a mature discipline, characterized by its simple mathematical description, which provides many powerful image analysis tools [4, 5]. Current applications of MM include, among others, geoscience and remote sensing, biological and medical imaging, industrial applications, identification and security control, and image coding [5].

Based on set theory, binary morphology was established by introducing fundamental operators applied to two sets [6, 7]. One set is processed by another having a carefully selected shape and size, known as the structuring element (SE), which is translated over the image. The SE acts as a probe for extracting or suppressing specific structures of the image objects, checking that each position of the SE fits within the image objects. Based on these ideas, two fundamental operators are defined in MM, namely *erosion* and *dilation* [3]. The application of the erosion operator to an image yields an output image, which shows where the SE *fits* the objects in the image. On the other hand, the application of the dilation operator to an image produces an output image, which shows where the SE *hits* the objects in the image. All other MM operations can be expressed in terms of erosion and dilation [8]. For instance, the notion behind the *opening* operator is to dilate an eroded image in order to recover as much as possible of the eroded image. In contrast, the *closing* operator erodes a dilated image so as to recover the initial shape of image structures that have been dilated. The filtering properties of the opening and closing are based on the fact that, depending on the size and shape of the

considered SE, not all structures from the original image will be recovered when these operators are applied [9]. Due to the nonlinear properties of MM filters, their application generally results in an irreversible, though controlled, loss of information.

Binary MM operators have been extended to gray-tone (mono-channel) images by viewing these data as an imaginary topographic relief; in this regard, the brighter the gray tone, the higher the corresponding elevation [10]. It follows that, in grayscale morphology, each 2-D gray tone image is viewed as if it were a digital elevation model (DEM). In practice, set operators directly generalize to gray-tone images. For instance, the intersection  $\cap$  (respectively, union  $\cup$ ) of two sets becomes the point-wise minimum  $\wedge$  (respectively, maximum  $\vee$ ) operator [11]. In a similar way to the binary case, specific image structures are extracted/suppressed according to the chosen SE. The latter is usually “flat” in the sense that it is defined in the spatial domain of the image (the  $x - y$  plane) [5].

The extension of the concepts of binary and grayscale MM to multi-channel imagery is not straightforward [12, 13]. In particular, multi-channel MM has received considerable attention in remote sensing applications, where the image data is frequently defined by vector valued pixels such as the quantity of energy for different wavelengths [14]. In hyperspectral imaging, for instance, hundreds of images corresponding to different wavelength channels are collected by an airborne/satellite image spectrometer for the same area on the surface of the Earth [15, 16]. With such a spectral resolution, the ability to detect and identify individual materials or land-cover classes is greatly enhanced in relation to other techniques available such as multispectral imaging, which only typically contains tens of images [17].

A simple approach to multi-channel MM in the literature consists in applying single-channel MM techniques to each channel separately (marginal MM) [18]. However, the marginal approach is unacceptable in remote sensing because, when MM techniques are applied independently to each image channel, there is a possibility for loss or corruption of information of the image due to the probable fact that new spectral constituents —not present in the original image— may be created as a result of processing the channels separately [13]. In addition, no correlation between spectral components is taken into account in the single-channel approach. An alternative way to approach the problem of multi-channel MM is to treat the data at each pixel as a vector. Unfortunately, there is no unambiguous means of defining the minimum and maximum values between two vectors of more than one dimension, and thus it is important to define an appropriate arrangement of vectors in the selected vector space.

Several vector-ordering schemes have been discussed in the literature [19]. The choice between the different available options is application-driven.

Four classes of ordering methods (marginal, reduced, partial and conditional ordering) will be shortly illustrated here in the context of hyperspectral imaging. Let us consider a hyperspectral image  $f$ , defined on the  $N$ -dimensional continuous space, where  $N$  is the number of spectral channels. Let  $f(x, y)$  and  $f(x', y')$  denote two pixels of the image, with  $f(x, y) = [f_1(x, y), \dots, f_N(x, y)]^T$  and  $f(x', y') = [f_1(x', y'), \dots, f_N(x', y')]^T$ . In marginal ordering (M-ordering), each pair of observations  $f_i(x, y)$  and  $f_i(x', y')$  is ordered independently along each of the  $N$  channels [20]. In reduced ordering (R-ordering), a scalar parameter function  $g$  is computed for each pixel of the image and the ordering is performed according to the resulting scalar values [18]. The ordered vectors satisfy the relationship  $f(x, y) \leq f(x', y') \Rightarrow g[f(x, y)] \leq g[f(x', y')]$ . In partial ordering (P-ordering), the input multivariate samples are partitioned into smaller groups, which are then ordered. Both R-ordering and P-ordering may lead to the existence of more than one suprema (or infima) and, thus, introduce ambiguity in the resulting data. In conditional ordering (C-ordering), the pixel vectors are initially ordered according to the ordered values of one of their components, e.g. the first component,  $f_1(x, y)$  and  $f_1(x', y')$ . As a second step, vectors that have the same value for the first component are ordered according to the ordered values of another component, e.g. the second component,  $f_2(x, y)$  and  $f_2(x', y')$ , and so on [21]. This type of ordering is not generally appropriate for remotely sensed data, where each spectral feature *as a whole* contains relevant information about the optical and physical properties of the observed land-cover [17]. In addition, pixel vectors in remote sensing are usually affected by atmospheric and illumination interferers, which may introduce fluctuations in the amount of energy, collected by the sensor at the different wavelength channels. The incident signal is electromagnetic radiation that originates from the sun and is measured by the sensor after it has been reflected upwards by materials on the surface of the Earth. As a result, two differently illuminated pixels that belong to the same spectral constituent may be ordered inconsistently by the C-ordering and M-ordering schemes.

In order to define appropriate vector ordering schemes for remote sensing applications, it is important to take into account the requirements of available techniques for analyzing data of interest. These can either inherently be full-pixel techniques or mixed-pixel techniques [16]. The underlying assumption governing full-pixel techniques is that each pixel vector measures the response of one predominantly underlying material at each site in a scene. In contrast, the underlying assumption governing mixed-pixel techniques is that each pixel vector measures the response of multiple underlying materials at each site. For example, mixed pixels in hyperspectral imagery exist for one of two reasons.

First, if the spatial resolution of the sensor is low enough for disparate materials to jointly occupy a single pixel, the resulting spectral measurement will be some composite of the individual spectra. This is the case for remote sensing platforms flying at high altitude. Secondly, mixed pixels can result when distinct materials are combined into a homogeneous mixture. This circumstance occurs independent of the spatial resolution of the sensor [17]. Spectral unmixing is the procedure in which the measured spectrum of a mixed pixel is decomposed into a collection of spectrally pure constituent spectra, or *endmembers*, and a set of correspondent fractions, or *abundances*, that indicate the proportion of each endmember present in the pixel [22]. Hence, a pursued goal in hyperspectral applications is to define a vector ordering scheme based on the spectral purity of the pixels, i.e., the supremum should be the “most spectrally pure” pixel, whereas the infimum should be the “most highly mixed” element.

The distance-driven ordering technique proposed in this chapter is based on ordering input vectors over the sum of the values obtained by calculating a spectral-based distance between a certain sample and all the other ordered ones. This means that the procedure above must be repeated for all the considered samples, i.e., each sample is compared to all the other ones by means of a spectral-based distance, and a final selection is made according to the resulting distance scores obtained for every different sample. This type of ordering (D-ordering) [23], which can be seen as a special class of R-ordering, has been found to be very effective in capturing both spatial and spectral variability in hyperspectral data, according to previous studies [24, 25]. The ambiguity is that the above cumulative distance is not injective in general, i.e., two or more distinct vectors may output the minimum or maximum distance. A solution suggested in the literature is to break the tie by taking into account positions of these vectors at the filter window [19]. Again, arbitrary decisions cannot be avoided. Another solution is to define an *ad hoc* total ordering for a vector space [26]. For example, by using a space-filling curve such as a Peano curve [27, 28], a total ordering is achieved since any two points on the vector space are ordered along the curve. However, the total ordering thus imposed is rather artificial and lacks physical interpretation.

In this chapter, we explore a more physically meaningful approach, based on applying dimension reduction techniques to bring the data from a high order dimension to a low order dimension [29]. We propose to break ties by looking at the spectral properties of the data in the reduced feature space constructed from the input channels. This observation is achieved after applying component transformations which aim to increase the spectral separability of the different land-cover classes. The remainder of this chapter is organized as follows. Section 2 describes the approach followed for extension of MM operations to hyperspectral imagery, and provides several processing

examples. Section 3 describes an application of extended MM operations for endmember extraction. The proposed technique is compared to other existing approaches using hyperspectral data collected by the NASA/JPL Airborne Visible-Infrared Imaging Spectrometer (AVIRIS) [15]. Section 4 describes a parallel implementation of the proposed technique to speed up its computational performance. The last section concludes with remarks and hints at plausible future research.

## 2. Multi-channel morphological transformations

Our attention in this section focuses primarily on the development of a mechanism to extend mono-channel MM operations to hyperspectral image data. The greatest challenge in the task of extending MM operations to multi-channel images is the definition of a vector ordering relation that allows for the determination of the maximum and minimum elements in any family of  $N$ -dimensional ( $N$ -D) vectors. In order to obtain the desired performance, we test the following approach: First, a lattice structure is imposed onto the spectral space by the definition of a distance measure, and, second, MM operations are defined by extension [24, 30]. Next, we provide a mathematical formulation for the extension of classic MM operations to multi-channel imagery. The section ends with some simple examples that illustrate the behavior of MM operations.

### 2.1. Mathematical formulation

The two basic operations of mathematical morphology are erosion and dilation. Following a usual notation [31], let us consider a grayscale image  $f$ , defined on a space  $E$ . Typically,  $E$  is the 2-D continuous space  $R^2$  or the 2-D discrete space  $Z^2$ . In the following, we refer to morphological operations defined on the discrete space. The flat erosion of  $f$  by  $B \subset Z^2$  is given by the following expression,

$$(f \ominus B)(x, y) = \text{Min}_{(s,t) \in Z^2(B)} \{f(x+s, y+t)\}, \quad (x, y) \in Z^2, \quad (1)$$

where  $Z^2(B)$  denotes the set of discrete spatial coordinates associated to pixels lying within the neighborhood defined by a flat SE, designed by  $B$ . Similarly, the flat dilation of  $f$  by  $B$  is given by

$$(f \oplus B)(x, y) = \text{Max}_{(s,t) \in Z^2(B)} \{f(x-s, y-t)\}, \quad (x, y) \in Z^2. \quad (2)$$

It should be noted that the two definitions above assume that the origin of the SE is at its center [5]. In order to extend the above basic morphological operations to hyperspectral images, let us now consider an image  $f$ , defined on the N-D space. We impose an ordering relation in terms of spectral purity in the set of pixel vectors lying within a flat SE, designed by  $B$ , by defining a cumulative distance between one particular pixel  $f(x, y)$ , where  $f(x, y)$  denotes an N-D vector at discrete spatial coordinates  $(x, y) \in Z^2$ , and all the pixel vectors in the spatial neighborhood given by  $B$  ( $B$ -neighborhood) as follows:

$$D_B[f(x, y)] = \sum_s \sum_t \text{Dist}[f(x, y), f(s, t)], \quad \forall (s, t) \in Z^2(B), \quad (3)$$

where  $\text{Dist}$  is a linear point-wise distance measure between two N-dimensional vectors. As a result,  $D_B[f(x, y)]$  is given by the sum of  $\text{Dist}$  scores between  $f(x, y)$  and every pixel vector in the  $B$ -neighborhood. Based on the cumulative distance above, the flat extended erosion of  $f$  by  $B$  is based on the selection of the  $B$ -neighborhood pixel vector that produces the minimum value for  $D_B$ :

$$(f \ominus B)(x, y) = \arg\_ \text{Min}_{(s, t) \in Z^2(B)} \{D_B[f(x + s, y + t)]\}, \quad (x, y) \in Z^2, \quad (4)$$

where the  $\arg\_ \text{Min}$  operator selects the pixel vector is most highly similar, according to the linear distance  $\text{Dist}$ , to all the other pixels in the  $B$ -neighborhood. On other hand, the flat extended dilation of  $f$  by  $B$  selects the  $B$ -neighborhood pixel vector that produces the maximum value for  $D_B$ :

$$(f \oplus B)(x, y) = \arg\_ \text{Max}_{(s, t) \in Z^2(B)} \{D_B[f(x - s, y - t)]\}, \quad (x, y) \in Z^2, \quad (5)$$

where the  $\arg\_ \text{Max}$  operator selects the pixel vector that is most highly different, according to  $\text{Dist}$ , to all the other pixels in the  $B$ -neighborhood. It should be noted that the proposed extended operators are vector preserving, in the sense that no vector (constituent) that is not present in the input data is generated as a result of the extension process [13]. Also, it is important to emphasize that the  $\arg$  operators are essential to achieve the above goal. In multi-channel morphology, the minimum (respectively, maximum) is the pixel vector that minimizes (respectively, maximizes) the value of  $D_B$ . As a result,

a selection is required. Quite opposite, in greyscale morphology each pixel is given by a single value or digital number (DN) and, therefore, the selection of the minimum (respectively, maximum) pixel can be simply accomplished by calculating the minimum (respectively, maximum) DN value in the  $B$ -neighborhood. On other hand, the choice of Dist is a key topic in the resulting multi-channel ordering relation. In this work, we consider a widely used distance metric in hyperspectral analysis: the spectral angle mapper (SAM) [16]. For illustrative purposes, let us consider two pixel vectors,  $\mathbf{f}(x', y')$  and  $\mathbf{f}(x'', y'')$ . The SAM between the spectral signatures of the two pixel vectors above is given by the following expression:

$$\text{SAM}[\mathbf{f}(x', y'), \mathbf{f}(x'', y'')] = \cos^{-1} \left( \frac{\mathbf{f}(x', y') \cdot \mathbf{f}(x'', y'')}{\|\mathbf{f}(x', y')\| \|\mathbf{f}(x'', y'')\|} \right) \quad (6)$$

where  $f_i(x', y')$  and  $f_i(x'', y'')$  refer to the  $i$ -th component of pixel vectors  $\mathbf{f}(x', y')$  and  $\mathbf{f}(x'', y'')$ , respectively. It should be noted that the SAM measurement is invariant in the multiplication of the input vectors by constants and, consequently, is invariant to unknown multiplicative scalings that may arise due to differences in illumination and sensor observation angle [22]. Hence, the use of SAM as the standard distance metric allows us to impose a partial order relationship of the vectors within a SE in terms of their spectral purity. It is important to notice that several distinct pixel vectors may output the same value for the cumulative distance-based function  $D_B$ . For illustrative purposes, let us assume that  $\mathbf{f}(x', y')$  and  $\mathbf{f}(x'', y'')$  are two distinct pixel vectors in the  $B$ -neighborhood. Let us also assume that which produce the same cumulative distance value, i.e.,  $D_B[\mathbf{f}(x', y')] = D_B[\mathbf{f}(x'', y'')]$ . Then, a partial solution to the above problem is given by the following tiebreak approach:

- 1) Apply a dimension reduction transformation  $h$  to the original N-D data  $\mathbf{f}$ , aimed at increasing the spectral separability between the observed land-cover surfaces in the reduced feature space. Two widely used dimension reduction techniques are considered: Principal Components Analysis (PCA) and Maximum Noise Fraction (MNF). PCA computes orthogonal projections that maximize the amount of data variance, and yields a dataset in a new uncorrelated coordinate system [17]. MNF uses a similar approach that includes statistical models for the noise in order to optimize a signal-to-noise ratio (SNR) criterion [32]. In the two cases, a new M-D

dataset  $\mathbf{g} = h(\mathbf{f})$  is obtained, with  $M \leq N$  and the resulting  $M$  channels ordered in terms of decreasing information content. By virtue of the considered transformation, features not discernible in the original data may be evident in the reduced feature space.

- 2) Order the pixels by looking at their spectral properties in the reduced feature space. If we assume that  $\mathbf{g}(x', y') = [g_1(x', y'), \dots, g_M(x', y')]^T$  and  $\mathbf{g}(x'', y'') = [g_1(x'', y''), \dots, g_M(x'', y'')]^T$  are the correspondent representations of  $\mathbf{f}(x', y')$  and  $\mathbf{f}(x'', y'')$  in the reduced feature space, an alternative solution is to break possibly incorrect ties by using their respective representations in  $\mathbf{g}$ . Following available approaches in the literature, we examine three different alternatives:
  - a) *C-ordering in the reduced feature space* (CRFS) [21] — In this schema, the pixels are ordered according to the ordered values of their first component in the reduced feature space, i.e.,  $g_1(x', y')$  and  $g_1(x'', y'')$ . Vectors that have the same value for the first component are ordered according to the ordered values of the second component, i.e.,  $g_2(x', y')$  and  $g_2(x'', y'')$ , and so on. It should be noted that both MNF and PCA transformations produce decompositions ordered in terms of decreasing information content, with the first component containing the highest amount of information.
  - b) *D-ordering in the reduced feature space* (DRFS) [23] — This approach is based on the calculation of a cumulative distance value for each of the pixels in the reduced feature space. This is accomplished by applying a multi-channel MM operation such as  $(\mathbf{g} \oplus B)(x, y)$  or  $(\mathbf{g} \ominus B)(x, y)$ . Since  $\mathbf{g}(x', y')$  and  $\mathbf{g}(x'', y'')$  are located in the spatial neighborhood of  $\mathbf{g}(x, y)$  defined by  $B$ , a cumulative distance value will be calculated for each of the pixels by virtue of any of the two considered multi-channel MM operations. The pixels may now be ordered according to the ordered values of their respective cumulative distance values in the reduced feature space.
  - c) *R-ordering about the centroid in the reduced feature space* (RRFS) [21] — This approach is based on ordering of the multivariate reduced sample pixels  $\mathbf{g}(x', y')$  and  $\mathbf{g}(x'', y'')$  according to their distance to a pre-selected central location  $\mathbf{c}_B(x, y)$ , in such a case, the centroid of all the reduced multivariate samples which are located

in the spatial neighborhood of  $\mathbf{g}(x, y)$  defined by  $B$ . The centroid of the above population is calculated as follows

$$c_B(x, y) = \frac{1}{K} \sum_s \sum_t \mathbf{g}(x-s, y-t), \quad \forall (s, t) \in Z^2(B), \quad (7)$$

where  $K$  denotes the total number of elements in  $B$ . The pixels may now be ordered according to the following relations, where  $\text{Dist}$  is a spectral-based distance (in our case, the SAM distance).

$$\mathbf{f}(x', y') \leq \mathbf{f}(x'', y'') \Rightarrow \text{Dist}[\mathbf{g}(x', y'), c_B(x, y)] \leq \text{Dist}[\mathbf{g}(x'', y''), c_B(x, y)], \quad (8)$$

and

$$\mathbf{f}(x'', y'') \leq \mathbf{f}(x', y') \Rightarrow \text{Dist}[\mathbf{g}(x'', y''), c_B(x, y)] \leq \text{Dist}[\mathbf{g}(x', y'), c_B(x, y)], \quad (9)$$

To conclude this section, we emphasize that the proposed tiebreak approach represents a partial solution to the problem since ties in the reduced feature space may still occur. However, we have experimentally tested that the percentage of ties in both PCA and MNF reduced feature spaces is significantly smaller than the percentage of ties found in the original N-D space, as it will be shown in experimental results.

## 2.2. Processing examples

In order to illustrate the proposed approach of extending MM operations to multi-channel image data, let  $B$  be a flat 3x3-pixel SE and let  $\mathbf{f}$  be a hyperspectral scene, collected by the DLR ROSIS imaging spectrometer [33] over a particular scenario: The so-called ‘Dehesa’ ecosystem, mainly formed by cork-oak trees, soil and pasture, in Caceres, SW Spain. Representative spectral signatures of cork-oak trees, pasture and soil, selected from the above data set, are shown in Fig. 1. The full hyperspectral scene consists of 88x134 high-resolution pixels of 1.2 meters, each containing 92 spectral bands covering the spectral range from 504-864 nm. The result of applying an extended erosion/dilation operation to  $\mathbf{f}$  using  $B$  is a new data cube, with exactly the same dimensions as the original, where each pixel is replaced by the maximum/minimum of the neighborhood defined by the flat SE. Fig. 2(a) illustrates the spectral band collected at 584 nm wavelength by the ROSIS imaging spectrometer. Figs. 2(b) and 2(c) show the band at 584 nm of the

resulting images after applying an extended dilation  $f \oplus B$ , and erosion  $f \otimes B$ , respectively. In both cases, DRFS ordering in a reduced feature space constructed by using the MNF transform was used to break cumulative distance ties. For comparative purposes, Figs. 2(d) and 2(e) respectively show resulting images obtained after applying mono-channel grayscale MM dilation and erosion to the spectral band collected at 584 nm wavelength by the ROSIS imaging spectrometer. As can be seen, flat dilation develops objects which appear as bright areas in the above spectral channel [see Fig. 2(a)], whereas flat erosion shrinks the bright objects and develops the dark areas in the same channel, regardless of the spectral purity of the samples.

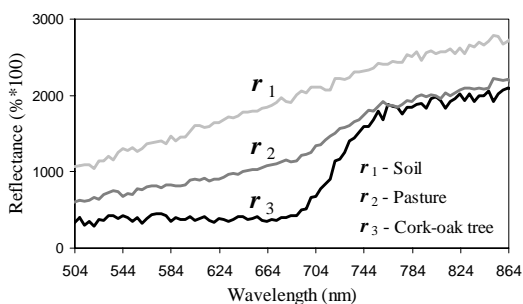


**Figure 1.** Representative spectral signatures for the main constituents present in a ROSIS hyperspectral image over a Dehesa test site in Caceres, SW Spain: Soil ( $r_1$ ), Pasture ( $r_2$ ) and Cork-oak tree ( $r_3$ ).

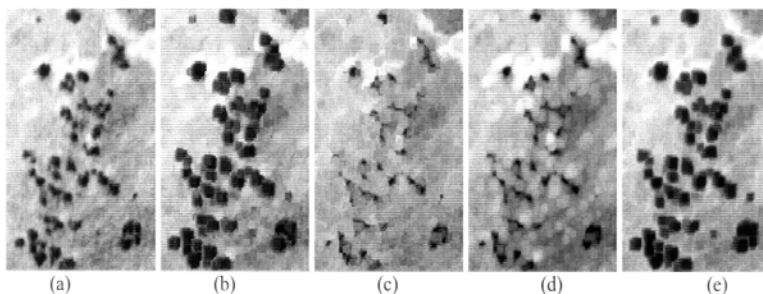


**Figure 2.** (a) Spectral band at 584 nm of a ROSIS hyperspectral image. (b) Spectral band at 584 nm of the hyperspectral image obtained after applying a multi-channel erosion to (a) using a flat 3x3 SE. (c) Spectral band at 584 nm of the hyperspectral image obtained after applying a multi-channel dilation to (a) using a flat 3x3 SE. (d) Resulting image after applying a mono-channel dilation to (a) using a flat 3x3 SE. (e) Resulting image after applying a mono-channel erosion to (a) using a flat 3x3 SE.

As can be examined in Fig. 2(b), extended dilation has the effect of expanding zones with “pure” spectral signatures (in the example, cork oak and soil areas are developed). Most of the gray-tone areas in Fig. 2(a) are made up of mixtures of soil and pasture because of the early growth stage of pasture at the time of sensor data acquisition (July 2001), a fact that was observed during a visit to the test site. This effect can be noticed in Fig. 2(c), where the erosion operation expands gray-tone (“mixed”) areas and shrinks both dark (cork-oak) and bright (pure soil) areas. It should be noted that the percentage of ties found by DRFS in the original N-D space in the above experiment was 4.32%, a moderately high score mainly caused by the similarity between different pixel vectors in different areas of the scene. By comparing each pair of tying signatures with representative spectral signatures in Fig. 1 using the SAM distance, we could perform a more detailed analysis about the nature of the ties. Specifically, we observed that most DRFS-based ties took place in soil and cork-oak areas (1.61% and 1.97%, respectively), while a smaller fraction of DRFS-based ties (0.74%) was found in pasture areas. From the above simple experiment we can conclude that, in this example, most of the ties found after applying DRFS to the original N-D space occurred in areas dominated by pure pixels. Quite opposite, the overall percentage of ties found by DRFS in the reduced MNF-based space was only 1.19%. Interestingly, ties in the reduced space were found to be more abundant in mixed pasture areas (0.62%) as compared to pure cork-oak (0.31%) and soil (0.26%) areas. This seems to indicate that most of the conflictive ties in the pure areas could be resolved by the MNF transform. Taking in mind that pasture areas dominate the ROSIS scene [see Fig. 2(a)], and that the percentage of ties in those areas was also decreased, the results above provide some objective confirmation of our introspection: that although ties in the reduced feature space may still occur, they are not so relevant as those found in the original N-D space in terms of our morphological description of the scene, based on the spectral purity of the samples. In order to anticipate some hints on the performance/applicability of CRFS, DRFS and RRFS, Table 1 provides a percentage-wise summary of the number of ties found after applying the three methods above to PCA- and MNF-reduced versions of the ROSIS image, as compared to the number of ties found in the original N-D space. As Table 1 reveals, all PCA- and MNF-based ordering methods were able to significantly reduce the number of ties in the original image, with both DRFS and RRFS resulting in a more significant reduction when combined with the MNF transform. Although a decrease in the number of ties does not necessarily imply better analysis accuracy, experimental results in the following section reveal that both DRFS and RRFS ordering strategies lead to improved classification results in endmember extraction applications.

**Table 1.** Overall and per-class percentage of ties found after applying CRFS, DRFS and RRFS ordering to a ROSIS hyperspectral image (no reduction), and to PCA- and MNF-reduced versions of the image.

| Class          | Original image |      |      | PCA-reduced image |      |      | MNF-reduced image |      |      |
|----------------|----------------|------|------|-------------------|------|------|-------------------|------|------|
|                | CRFS           | DRFS | RRFS | CRFS              | DRFS | RRFS | CRFS              | DRFS | RRFS |
| Soil           | 2.03           | 1.61 | 1.52 | 1.23              | 0.42 | 0.83 | 1.12              | 0.26 | 0.51 |
| Cork-oak trees | 1.58           | 1.97 | 2.04 | 1.26              | 0.31 | 0.75 | 0.92              | 0.31 | 0.62 |
| Pasture        | 1.62           | 0.74 | 1.03 | 1.53              | 0.75 | 1.09 | 1.41              | 0.62 | 0.95 |
| Overall        | 5.23           | 4.32 | 4.59 | 4.02              | 1.48 | 2.67 | 3.45              | 1.19 | 1.98 |

### 3. Extended morphological operations for endmember extraction

In previous research, several efforts have been made towards the application of morphological analysis to multi/hyperspectral image analysis from the perspective of a pure pixel classification [34, 35, 36]. In this section, we introduce a morphological approach to mixed pixel analysis of hyperspectral imagery based on multi-channel MM operations. Linear spectral unmixing (LSU) is one of the most successful techniques in the literature [16, 22] to characterize mixed pixels. Let  $f(x, y)$  be a mixed pixel at spatial coordinates  $(x, y)$ . In the LSU approach, the mixed pixel is modeled in terms of a linear combination of macroscopically pure endmember materials  $e_i, i = 1, \dots, E$ , according to the equations and constraints below [37]:

$$f(x, y) = \sum_{i=1}^E \Phi_i(x, y) \cdot e_i, \quad \sum_{i=1}^E \Phi_i(x, y) = 1, \quad 0 \leq \Phi_i(x, y) \leq 1, \quad (10)$$

where  $\Phi_i(x, y)$  is a scalar value representing the fractional coverage of endmember vector  $e_i$  in the pixel at spatial location  $(x, y)$ . Then, the key task in LSU is to find an appropriate suite of endmember pixels in the scene, which are then used to model mixed pixel spectra through a linear combination of endmember spectral signatures.

Over the past decade, several algorithms have been proposed for the purpose of deriving image endmembers from hyperspectral scenes. One of the most successful approaches has been the pixel purity index (PPI) algorithm [38], which first applies an MNF reduction to the original data and then

proceeds by generating a large number  $L$  of random  $N$ -D vectors, also called “skewers”, through the dataset. Every data point is projected onto each skewer, and the data points that correspond to extrema in the direction of a skewer are labeled as endmembers after an educated “trial and error” approach [39]. Another standard technique is the  $N$ -FINDR algorithm, which aims at identifying the set of pixels which define the simplex with the maximum volume, potentially inscribed within the dataset [40]. In the Convex cone analysis (CCA) method, spectral vectors are expressed as linear combinations of nonnegative components, which lie inside a nonnegative, convex region. The objective of CCA is to find the boundary vectors for that region, which are then used as endmembers for spectral unmixing [41]. Opposite to the PPI,  $N$ -FINDR and CCA algorithms, which might be characterized as different instances of a similar technique based on the search for spectral convexities in  $N$ -D space, the Naval Research Laboratory’s Optical real-time adaptive identification system (ORASIS) uses a process called exemplar selection that rejects redundant spectra by calculating the SAM distance between spectral vectors. Any vector that is not separated by a certain threshold angle  $TA$  from all the exemplars is removed from the data [42]. It is clear that all the endmember selection methods addressed above handle the data not as an image but as an unordered listing of spectral measurements where the spatial coordinates can be shuffled arbitrarily without affecting analysis. However, one of the distinguishing properties of hyperspectral data, as collected by available imaging spectrometers, is the multivariate information coupled with a two-dimensional (2-D) pictorial representation amenable to image interpretation. Subsequently, there is a need to incorporate the image representation of the data in the development of appropriate endmember extraction techniques.

Before introducing our own approach to endmember extraction, we list key advantages in the use of multi-channel MM operations to perform the above task. A first major point is that, contrary to abundance estimation, endmember extraction is basically a non-linear task. Furthermore, MM allows for the introduction of a joint spatial/spectral approach in the search for endmembers. This type of processing can be applied to the search of spectral convexities and to the use of the spatial arrangement between the pixels. Endmembers can be identified by following an iterative process where pixels in close proximity in the spatial domain compete against each other in terms of their convexity or spectral purity. As a result, extended MM operations allow for the determination of a local representative in a neighborhood that will be compared to other locally selected pixels. As a final note, MM operations are implemented by replacing a pixel with a neighbor that satisfies a certain condition. In grayscale morphology, the condition is related to the digital value of the pixel, and dilation and erosion are respectively based on the replacement

of a pixel by the neighbor with the maximum and minimum digital value. Since an endmember can be defined as a spectrally pure pixel that is used to describe other mixed pixels in the scene [22], multi-channel MM operations can obviously contribute to locating suitable pixels that replace others in the scene according to some desired particularity of the pixel, for example, its spectral purity.

### 3.1. Automated morphological endmember extraction

We develop in this section a morphological approach to endmember extraction, which focuses on the analysis of spatial and spectral patterns simultaneously [24]. Fig. 3 presents a general block diagram of the proposed approach, called automated morphological endmember extraction (AMEE). The input to the AMEE method is the full data cube, with no previous dimensionality reduction or pre-processing. Parameter  $I$  refer to the number of iterations that the algorithm performs. Parameters  $B_{\min}$  and  $B_{\max}$  respectively denote the minimum and maximum SE sizes that will be considered in the iterative process. These parameters are interrelated, as the number of iterations depends on the minimum and maximum SE sizes under scrutiny. For the proposed method, disk SE's of increasing radius were constructed. Firstly, a pixel-level morphological eccentricity index (MEI) is initialized to the value 0 for all the pixels in the image. Then, the minimum disk element  $B = B_{\min}$  is selected and moved through all the pixels of the image. The maximum ("spectrally purest") and the minimum ("most highly spectrally mixed") pixels are obtained at each  $B$ -neighborhood by multi-channel dilation and erosion operations. The MEI associated to the purest pixel is updated by the resulting score after comparing the result of the dilation to the result of erosion [43]. Let  $(x', y')$  be the spatial coordinates of the maximum pixel at the  $B$ -neighborhood of a certain pixel  $f(x, y)$ . Similarly, let  $(f \ominus B)(x, y)$  be the minimum pixel of the same kernel neighborhood. Then, the MEI score at  $(x', y')$  is updated by using the following expression:

$$\text{MEI}(x', y') = \text{MEI}(x', y') + \text{Dist}[(f \oplus B)(x, y), (f \ominus B)(x, y)], \quad (11)$$

where  $\text{Dist}$  is the SAM distance. It should be noted that, by means of the above definition, the pixel at spatial coordinates  $(x', y')$ , i.e.,  $f(x', y')$ , may be the maximum pixel at the neighborhood of two or more pixels. When this happens, the value of  $\text{MEI}(x', y')$  is uniquely defined as the sum of the  $\text{Dist}$  scores between  $f(x', y')$  and the minimum pixel in the neighborhood of each of the

pixels above. As a result, if  $f(x', y')$  is selected several times as a maximum pixel, then its associated MEI score will be increased according to the number of times it was selected. The previously described operation is repeated by using disk SE's of progressively increased radius, and the algorithm performs as many iterations as needed until  $B = B_{\max}$  is achieved.

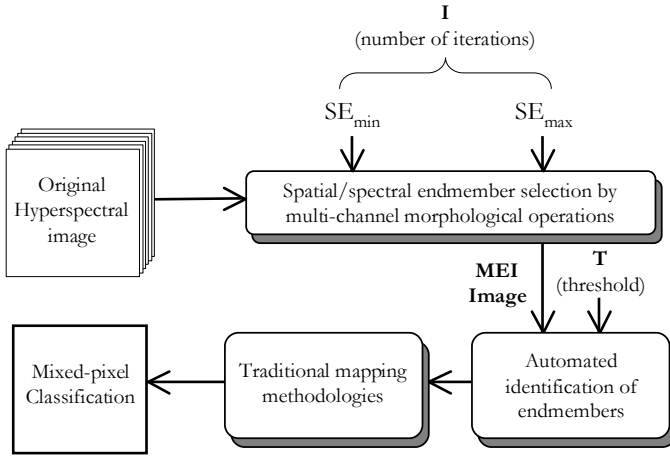


**Figure 3.** General architecture of the proposed endmember extraction approach.

It should be noted that the consideration of several SE sizes is very important in order to neglect pixels that are not sufficiently pure, and to preserve those pixels which are sufficiently pure but located very close to other pixels with higher degree of purity. In previous research, we experimentally proved that small SE's tend to propagate mixed pixels as well as pure pixels, while large SE's can result in the loss of important endmembers [30]. In order to overcome the above limitations and reduce the sensitivity of the proposed method to parameter selection, we introduced the competitive multi-scale approach above for the calculation of the MEI index, with satisfactory results in a variety of applications [24]. Automated endmember selection is performed from the MEI image obtained in the competitive endmember selection step by using a threshold value  $T$ , which results from using the multi-level Otsu method, an automated approach based on the minimization of the weighted sum of group variances [44]. The final selection is refined by a region-growing procedure incorporating neighboring pixels that are spectrally similar to the regions obtained after thresholding. Mean spectra are obtained from the resulting regions after the region-growing process. As a consequence, a final

set of endmembers is obtained. Traditional methodologies such as fully constrained LSU [37] can be used for the purpose of mapping the obtained endmembers over the original image, thus obtaining a final classification result in terms of endmember fractional abundances in the mixed pixels.

### 3.2. Quantitative assessment of endmember extraction techniques

This section describes a series of experiments that use real hyperspectral data to conduct a comprehensive comparison between standard endmember extraction algorithms. An AVIRIS imaging spectrometer dataset collected over the Jasper Ridge Biological Preserve (JRBP) in California [see Fig. 4(a)] has been selected for experiments due to the availability of ground-truth image endmembers for this scene. The dataset, acquired on April 1998, consists of 512x614 pixels and 224 spectral bands, with a nominal ground resolution of 20 m, spectral resolution of 10 nm, and 16-bit radiometric resolution. In a previous study of surface materials over JRBP, image endmembers were derived from the scene above based on extensive ground studies [45]. Fig. 4(b) plots spectral signatures associated to the main constituent materials at JRBP (water vapor bands and low SNR bands were removed to reduce noise). These signatures, denoted as  $s_1$  (soil),  $s_2$  (evergreen forest),  $s_3$  (dry grass),  $s_4$  (chaparral vegetation) and  $s_5$  (lake water), will be used as reference spectral signatures in a quantitative and comparative assessment of endmember extraction algorithms.

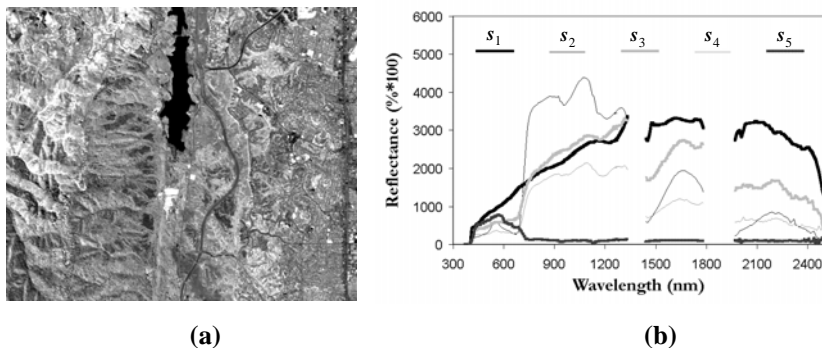


**Figure 4.** (a) Spectral band at 903 nm of an AVIRIS hyperspectral image collected over the Jasper Ridge biological preserve in California. (b) Ground-truth endmember signatures: Soil ( $s_1$ ), evergreen forest ( $s_2$ ), dry grass ( $s_3$ ), chaparral vegetation ( $s_4$ ), and lake water ( $s_5$ ).

In order to obtain the best performance from each alternative method tested, we have optimized parameter values as follows, bearing in mind that the N-FINDR and CCA do not require any input parameters. We first observed that PPI produced the same final set of endmembers for the JRBP real scene when the value of  $L$  was 3000 iterations or above (values of  $L=10^4$ ,  $L=10^5$  and  $L=10^6$  iterations were tested). Based on the above simple experiment,  $L$  was set to 3000 iterations, which is in accordance with other experiments in the literature [31]. In contrast, the developers of the ORASIS method at NRL optimized each running algorithm by carefully setting the TA parameter to an appropriate value. This was done by taking into account the SNR of the dataset [46]. Finally, a previous performance study of our AMEE algorithm using simulated multi-channel image datasets revealed that satisfactory results in most situations can be found by setting  $S_{\min}$  and  $S_{\max}$  parameters to 3- and 15-pixel radius disk SE's respectively [25]. These values were also found appropriate for the JRBP scene used in this work, mainly due to the observed width in pixels of patterns of interest in the data.

An experiment-based cross-examination of PPI, N-FINDR, CCA, ORASIS and AMEE in the task of extracting endmembers from real hyperspectral data is conducted by using the JRBP scene above. As in the previous application, six different combinations were tested in the construction of multi-channel morphological operations used by AMEE, namely MNF+CRFS, MNF+DRFS, MNF+RRFS, PCA+CRFS, PCA+DRFS, and PCA+RRFS. Table 2 tabulates the spectral similarity scores produced by SAM for extracted endmembers from JRBP, using selected image endmembers in

**Table 2.** SAM scores between image endmembers, produced by PPI, N-FINDR, CCA, ORASIS and AMEE methods, and ground-truth spectral signatures measured at the Jasper Ridge biological preserve in California.

| Method          | $s_1$ | $s_2$ | $s_3$ | $s_4$ | $s_5$ |
|-----------------|-------|-------|-------|-------|-------|
| PPI             | 0.027 | 0.022 | 0.021 | 0.019 | 0.017 |
| N-FINDR         | 0.028 | 0.025 | 0.022 | 0.020 | 0.019 |
| CCA             | 0.032 | 0.024 | 0.026 | 0.020 | 0.022 |
| ORASIS          | 0.032 | 0.021 | 0.025 | 0.017 | 0.020 |
| AMEE (MNF+CRFS) | 0.017 | 0.019 | 0.018 | 0.021 | 0.016 |
| AMEE (MNF+DRFS) | 0.009 | 0.007 | 0.008 | 0.006 | 0.008 |
| AMEE (MNF+RRFS) | 0.013 | 0.010 | 0.012 | 0.014 | 0.015 |
| AMEE (PCA+CRFS) | 0.016 | 0.018 | 0.015 | 0.022 | 0.017 |
| AMEE (PCA+DRFS) | 0.011 | 0.012 | 0.010 | 0.009 | 0.011 |
| AMEE (PCA+RRFS) | 0.014 | 0.013 | 0.013 | 0.016 | 0.016 |

Fig. 4(b) as ground-truth information. Results in Table 2 reveal that all tested methods produce endmembers that are similar, in spectral terms, to the reference signatures for the five materials studied. However, when the MNF+DRFS combination is used, AMEE endmembers clearly provide the best similarity scores in the five materials under scrutiny. Nonetheless, MNF+RRFS, PCA+DRFS and PCA+RRFS also produce very accurate results. Finally, when CRFS ordering is used, AMEE still produces results that are slightly better than those found by PPI, N-FINDR, CCA and ORASIS in four of the five materials. Only the chaparral vegetation constituent ( $s_4$ ) is characterized more effectively by ORASIS, a purely spectral method. One explanation for this result might be that the spatial trend of the chaparral vegetation component in the real scenes follows a very irregular pattern, not necessarily correlated as observed in the spatial distribution of the other studied endmembers [45]. Another reason might be the high spectral similarity of  $s_4$  with respect to other vegetation endmembers such as  $s_2$  and  $s_3$  [see Fig. 4(b)]. The results above indicate that the integrated use of spatial and spectral information, accomplished by multi-channel MM operations, improves the selection of endmembers for spectral unmixing applications. It is noteworthy to state, however, that there are certain cases where the LSU model may not be flexible enough to accommodate the full range of natural vegetation structure throughout the observed landscape, due to the presence of non-linear effects caused by multiple scattering of photons [22]. Further work is required to characterize such effects using non-linear models.

## 4. Parallel implementation

A drawback in the morphological approach described in the previous section has to do with the need to heed a range of morphological filters with increasing SE sizes, a labor which results in a heavy computational burden when processing high-dimensional data. This phenomenon is particularly relevant for the case of images with large and spectrally homogeneous regions. In this section, we describe AMEEPAR, a parallel version of the AMEE algorithm. First, we provide a description of the parallel algorithm and then we illustrate its parallel performance on a supercomputer facility at NASA's Goddard Space Flight Center.

### 4.1. Parallel morphological endmember extraction

Before describing the parallel algorithm, we should point out that it has been implemented as an extension of classic mesh-based parallel techniques [47]. To reduce code redundancy and enhance reusability, our goal was to reuse much of the code for the sequential algorithm in the parallel implementation. For that purpose, we implemented a spatial-domain

decomposition partitioner (SDP) module that subdivides the image into multiple blocks made up of entire pixel vectors, and assigns one or more blocks to each processing element (PE) as shown in Fig. 5. There are several reasons that justify the above decision. First, the application of spatial-domain partitioning is a *natural approach* for low level image processing, as many operations require the same function to be applied to a small set of elements around each data element present in the image data structure. A second reason has to do with the cost of inter-processor communication. In spectral-domain parallel, the SE-based calculations made for each hyperspectral pixel need to originate from several PEs, and thus require intensive inter-processor communication.

In the following, we will refer to each partial data structure produced by the proposed SDP module as a parallelizable spatial/spectral partition (PSSP). Thus, a PSSP can be defined as a hyperspectral data partition that can be processed independently, without communication. In other words, all data accesses in a PSSP must refer to the data local to the processing unit executing the operation. In order to achieve the above goal, it is necessary to handle border effects, and also to introduce an overlapping scatter at each partition. In our implementation, a function to update overlapping parts of partial data structures has been implemented in order to avoid inter-processor communication when the SE computation is split amongst several different processing nodes. It should be noted that such communication overhead

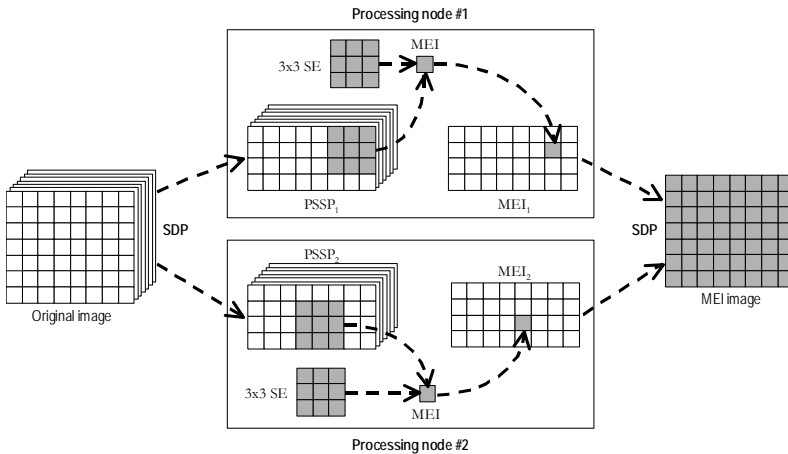


**Figure 5.** Example SE-based parallel morphological operation performed using two processing units.

prevents adequate exploitation of the concept of PSSP, since processing of a PSSP cannot be entirely accomplished at one single PE without communication. In order to eliminate such overhead, the proposed SDP module has been designed to allow overlapping between adjacent PSSPs, namely, a so-called *scratch* line is added to each of the adjacent PSSPs to avoid accesses outside their domain.

It should be noted that Fig. 5 gives a simplified view of the partitioning problem, as some steps of the operation are not shown. For example, depending on how many adjacent PSSPs are involved in the parallel computation of an SE, it may be necessary to place a *scratch border* around each PSSP to completely avoid inter-processor communication. In this regard, it is important to emphasize that the amount of redundant information introduced by the overlapping scatter depends on the size of  $B$ , the SE used in the morphological operations. However, our implementation of the AMEEPAR algorithm always uses a constant 3x3-pixel SE through the different iterations. Instead of increasing the size of the SE to consider a larger spatial neighborhood, we replace the original image cube  $f$  or, equivalently, the local PSSP in parallel processing, by the resulting cube after applying a dilation operation using  $B$ . This allows us to perform multi-scale analysis of the data without increasing the scratch border size between subsequent iterations [48].

## 4.2. Parallel performance evaluation

This subsection provides an assessment of parallel morphological endmember extraction in providing significant performance gains without loss of accuracy in the analysis of hyperspectral data. First, we provide an overview of the parallel computing architecture used for evaluation purposes. Second, a quantitative assessment of the proposed parallel approach is provided.

The parallel computing architecture used in experiments was the Thunderhead Beowulf cluster at NASA's Goddard Space Flight Center. It is composed of 256 dual 2.4 Ghz Intel Xeon nodes, each with 1 Gb of memory and 80 Gb of main memory. The total peak performance of the system is 2457.6 Gflops. Along with the 512-processor computer core, Thunderhead has several nodes attached to the core with 2 Ghz optical fibre Myrinet. The parallel algorithms tested in this work were run from one of such nodes, called thunder1. The operating system used at the time of experiments was Linux RedHat 8.0, and MPICH was the message-passing library used.

To empirically investigate the scaling properties of the considered parallel algorithm, Fig. 6 plots the speedup factors as a function of the number of available processors at Thunderhead. For illustrative purposes, only MNF-based reduction (followed by the three considered vector ordering strategies, namely, CRFS, DRFS and RRFS) were considered in experiments. Since the

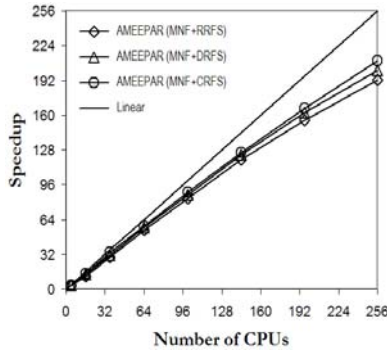


**Figure 6.** Parallel performance of AMEEMPAR on Thunderhead.

Jasper Ridge AVIRIS scene represents a large-sized problem dominated by mixed pixels, there is sufficient computation to gain an impact from a large number of processors in parallel computations. As a result, the dominant issue in AMEEMPAR experiments in this section is problem size, which makes the algorithm very appealing for high-dimensional imaging applications. Results in Fig. 5 reveal that the algorithm obtains good scalability (close to linear) in the Thunderhead computer. Although for a high number of nodes the speedup graphs flatten out a little, due to the relatively short execution times, they show significant improvement over a single-processor run in the same architecture. For illustrative purposes, Table 3 reports the algorithm processing times measured in Thunderhead using different numbers of processors. Interestingly, the table also shows that the utilization of parallel processing may allow highly accurate, near real-time endmember extraction very large and high-dimensional hyperspectral image scenes.

**Table 3.** Execution times (in seconds) achieved by the parallel morphological algorithm on Thunderhead.

| # CPUs | AMEEMPAR (MNF+CRFS) | AMEEMPAR (MNF+DRFS) | AMEEMPAR (MNF+RRFS) |
|--------|---------------------|---------------------|---------------------|
| 1      | 6136                | 6895                | 7094                |
| 4      | 2264                | 2337                | 2274                |
| 16     | 562                 | 613                 | 537                 |
| 36     | 222                 | 236                 | 227                 |
| 64     | 116                 | 127                 | 126                 |
| 100    | 76                  | 83                  | 82                  |
| 144    | 53                  | 58                  | 57                  |
| 196    | 41                  | 44                  | 44                  |
| 256    | 33                  | 36                  | 35                  |

## 5. Conclusions and future lines

This chapter has described new trends in efficient multi-channel morphological processing of hyperspectral imagery by simultaneously considering the spatial and spectral information. A physically meaningful partial vector organization scheme is introduced, and three different approaches (CRFS, DRFS and RRFS) are explored in order to alleviate the problem of multiple suprema (or infima) in morphological operations. Multi-channel filters are then used to develop a morphological endmember extraction technique which allows mixed-pixel characterization. Experimental results, using real hyperspectral data sets dominated by mixed pixels, demonstrate that the combined use of spatial and spectral information in the selection of endmembers improves the results found by available techniques that consider the spectral information alone. This goal can be achieved in near real-time by means of data partitioning-based parallel implementations.

As future research, we are currently working toward a systolic array-based VLSI design of the proposed morphological algorithms, susceptible of being implemented on field-programmable gate arrays (FPGAs) for real-time performance. A preliminary description of the above design, aimed at optimizing multi-channel morphological operations, can be found in [49]. Future work will also include the study of other distances (both linear and nonlinear) to be used in the extension of morphological operations, and the incorporation of non-linear mixture models. We will also carry out an investigation of additional strategies to reduce the impact of partial ordering in the vector space, without losing the physical interpretation inherent to the multi-channel remote sensing data.

## Acknowledgement

The author would like to gratefully thank Prof. Chein-I Chang for his guidance, encouragement and support during a research visit to his laboratory, Remote Sensing Signal and Image Processing Laboratory (RSSIPL). He would also like to thank J. Bowles and D. Gillis for their significant effort in the task of applying Naval Research Laboratory's ORASIS algorithm to the images discussed in this chapter, and M. Winter, for providing an evaluation version of N-FINDR algorithm that was used in experiments. Contributions by R. O. Green and J. A. Gualtieri, in the form of valuable comments to improve the proposed approaches, are also gratefully acknowledged. Last but not least, the author would like to express his gratitude to J. Chanussot and P. Soille for many interesting discussions on the usage of mathematical morphology in hyperspectral imaging.

## References

1. G. Matheron, *Eléments Pour une Théorie des Milieux Poreux*. Masson: Paris, 1967.
2. G. Matheron and J. Serra, "The birth of mathematical morphology," in *Proceedings of 6th International Symposium on Mathematical Morphology*, H. Talbot and R. Beare (Eds.), Sydney, Australia, 2002, pp. 1–16.
3. J. Serra, *Image Analysis and Mathematical Morphology*. Academic: New York, 1982.
4. J. Serra, *Image Analysis and Mathematical Morphology, Volume 2: Theoretical Advances*, J. Serra (Ed.). Academic: London, 1988.
5. P. Soille, *Morphological Image Analysis: Principles and Applications, 2nd ed.* Springer: Berlin, 2003.
6. J. Goutsias, H. Heijmans, "Fundamenta Morphologicae Mathematicae," *Fund. Inf.*, Vol. 41, pp. 1–30, 1999.
7. C. Ronse, "Set-theoretical algebraic approaches to connectivity in continuous or digital spaces," *Journal of Mathematical Imaging and Vision*, Vol. 8, pp. 41–58, 1998.
8. H. Heijmans, "Morphological image operators," in *Advances in Electronics and Electron Physics Series*. Academic: New York, 1994.
9. C. Ronse and H. Heijmans, "The algebraic basis of mathematical morphology: II. Openings and closings," *Comput. Vis., Graph., Image Process.: Image Understand.*, Vol. 54, pp. 74–97, 1991.
10. S.R. Sternberg, "Grayscale morphology," *Comput. Graph. Image Process.*, Vol. 35, pp. 333–355, 1986.
11. R.M. Haralick, S.R. Sternberg, and X. Zhuang, "Image analysis using mathematical morphology," *IEEE Trans. Pattern Anal. Machine Intell.*, Vol. 9, pp. 532–550, 1987.
12. M. Comer and E. Delp, "Morphological operations for color image processing," *J. Electron. Imag.*, Vol. 8, pp. 279–289, 1999.
13. G. Louverdis, M.I. Vardavoulia, I. Andreadis, Ph. Tsalides, "A new approach to morphological color processing," *Pattern recognition*, Vol. 35, pp. 1733–1741, 2002.
14. P. Soille and M. Pesaresi, "Advances in mathematical morphology applied to geoscience and remote sensing," *IEEE Trans. Geosci. Remote Sensing*, Vol. 40, pp. 2042–2055, 2002.
15. R.O. Green et al., "Imaging spectroscopy and the airborne visible/infrared imaging spectrometer (AVIRIS)," *Remote Sensing of Environment*, Vol. 65, pp. 227–248, 1998.
16. C.-I Chang, *Hyperspectral Imaging: Techniques for Spectral Detection and Classification*. Kluwer Academic Publishers, 2003.
17. X. Jia, J.A. Richards, and D.E. Ricken, *Remote Sensing Digital Image Analysis: An Introduction*. Springer: Berlin, 1999.
18. V. Barnett, "The ordering of multivariate data," *J.R. Statist. Soc. A.*, Vol. 139, pp. 318–355, 1976.
19. J. Astola, P. Haavisto, and Y. Neuvo, "Vector median filters," *Proc. IEEE*, Vol. 78, pp. 678–689, 1990.

20. I. Pitas and C. Kotropoulos, "Multichannel L filters based on marginal data ordering," *IEEE Trans. Signal Processing*, Vol. 42, pp. 2581–2595, 1994.
21. K. Tang, J. Astola, and Y. Neuvo, "Nonlinear multivariate image filtering techniques," *IEEE Trans. Image Processing*, Vol. 4, pp. 788–798, 1995.
22. N. Keshava and J.F. Mustard, "Spectral unmixing," *IEEE Signal Processing Magazine*, Vol. 19, pp. 44–57, 2002.
23. M. Pappas and I. Pitas, "Multichannel distance filter," *IEEE Trans. Signal Process.*, Vol. 47, pp. 3412–3416, 1999.
24. A. Plaza, P. Martinez, R. Perez, J. Plaza, "Spatial/spectral endmember extraction by multidimensional morphological operations," *IEEE Trans. Geosci. Remote Sensing*, Vol. 40, pp. 2025–2041, 2002.
25. A. Plaza, P. Martinez, R. Perez, J. Plaza, "A new approach to mixed pixel classification in hyperspectral imagery based on extended morphological profiles," *Pattern Recognition*, Vol. 37, pp. 1097–1116, 2004.
26. H. Talbot, C. Evans, and R. Jones, "Complete ordering and multivariate mathematical morphology," in *Computational Imaging and Vision*, J. Goutsias, L. Vincent, and D. Bloemberg (Eds.). Kluwer Academic Publishers, 2000, pp. 27–34.
27. J. Chanussot and P. Lambert, "Total ordering based on space filling curves for multivalued morphology," in *Mathematical Morphology and its Applications to Image and Signal Processing*, H. Heijmans and J. Roerdink (Eds.). Kluwer Academic Publishers, 1998, pp. 51–58.
28. C. Regazzoni and A. Teschioni, "A new approach to vector median filtering based on space filling curves," *IEEE Trans. Image Processing*, Vol. 6, pp. 1025–1037, 1997.
29. J. Goutsias, H. Heijmans, and K. Sivakumar, "Morphological operators for image sequences," *Comput. Vis. Image Understand.*, vol. 62, pp. 326–346, 1995.
30. A. Plaza, P. Martinez, J. Plaza, R. Perez, "Dimensionality reduction and classification of hyperspectral image data using sequences of extended morphological transformations," *IEEE Trans. Geosci. Remote Sensing*, Vol. 43, pp. 466–479, 2005.
31. A. Plaza, P. Martinez, R. Perez, J. Plaza, "A quantitative and comparative analysis of endmember extraction algorithms from hyperspectral data," *IEEE Trans. Geosci. Remote Sensing*, Vol. 42, pp. 650–663, 2004.
32. A. Green, M. Berman, P. Switzer, and M. Craig, "A transformation for ordering multispectral data in terms of image quality with implications for noise removal," *IEEE Trans. Geosci. Remote Sensing*, Vol. 26, pp. 65–74, 1988.
33. A. Müeller, A. Hausold, P. Strobl, "HySens–DAIS/ROSIIS imaging spectrometers at DLR," *Proc. VIII SPIE Intl. Symp. on Remote Sensing*, Toulouse, France, 2001.
34. M. Pesaresi and J. A. Benediktsson, "A new approach for the morphological segmentation of high resolution satellite imagery," *IEEE Trans Geosci. Remote Sensing*, Vol. 39, pp. 309–320, 2001.
35. J. A. Benediktsson, M. Pesaresi, and K. Arnason, "Classification and feature extraction for remote sensing images from urban areas based on morphological transformations," *IEEE Trans Geosci. Remote Sensing*, Vol. 41, pp. 1940–1949, 2003.
36. J. A. Palmason, J. A. Benediktsson, and K. Arnason, "Morphological transformations and feature extraction for urban data with high spectral and spatial

- resolution,” *Proc. IEEE Intl. Geosci. Remote Sensing Symp.*, Toulouse, France, 2003.
37. D. Heinz and C.-I Chang, “Fully constrained least squares linear mixture analysis for material quantification in hyperspectral imagery,” *IEEE Trans. Geosci. Remote Sensing*, Vol. 39, pp. 529–545, 2000.
  38. J. W. Boardman, F. A. Kruse, and R. O. Green, “Mapping target signatures via partial unmixing of AVIRIS data,” *Proc. VI NASA/JPL Airborne Earth Science Workshop*, PaSAMena, California, 1995.
  39. C. A. Bateson and B. Curtiss, “A method for manual endmember selection and spectral unmixing,” *Remote Sensing of Environment*, Vol. 55, pp. 229–243, 1996.
  40. M. E. Winter, “N-FINDR: An algorithm for fast autonomous spectral end-member determination in hyperspectral data,” *Proc. SPIE Imaging Spectrometry V*, Vol. 3753, pp. 266–275, 1999.
  41. A. Ifarraguerri and C.-I Chang, “Multispectral and hyperspectral image analysis with convex cones,” *IEEE Trans. Geosci. Remote Sensing*, Vol. 37, pp. 756–770, 1999.
  42. J. Bowles, D. Gillis, P. Palmadesso, “New improvements in the ORASIS algorithm,” *Proc. IEEE Aerospace Conference*, Big Sky, MT, 2000.
  43. A. Plaza, P. Martínez, J.A. Gualtieri, R. Perez, “Automated identification of endmembers from hyperspectral images using mathematical morphology,” *Proc. VIII SPIE Intl. Symp. Remote Sensing*, Toulouse, France, 2001.
  44. N. Otsu, “A threshold selection method from gray-level histograms,” *IEEE Trans. Syst., Man, Cybern.*, Vol. 9, pp. 62–66, 1979.
  45. M. Garcia and S. L. Ustin, “Detection of interannual vegetation responses to climatic variability using AVIRIS data in a coastal savanna in California,” *IEEE Trans. Geosci. Remote Sensing*, Vol. 39, pp. 1480–1490, 2001.
  46. R. O. Green, B. Pavri, J. Faust, and O. Williams, “AVIRIS radiometric laboratory calibration, inflight validation and a focused sensitivity analysis in 1998,” *Proc. VIII NASA/JPL Airborne Earth Science Workshop*, PaSAMena, California, 1999.
  47. A. Plaza, P. Martínez, J. Plaza, R.M. Perez, “Parallel implementation of algorithms for endmember extraction from AVIRIS hyperspectral imagery,” *Proc. XIII NASA/JPL Airborne Earth Science Workshop*, PaSAMena, California, 2004.
  48. D. Valencia, A. Plaza, P. Martínez, J. Plaza, “On the use of cluster computing architectures for implementation of hyperspectral analysis algorithms,” *Proc. X IEEE Symp. Computers and Communications*, Cartagena, Spain, 2005.
  49. P. L. Aguilar, A. Plaza, R. Perez, P. Martínez, “Morphological endmember identification and its systolic array design,” in *Neural Networks and Systolic Array Design*, D. Zhang and S.K. Pal (Eds.). World Scientific: Singapore, 2002, pp. 47–69.